Electronic Supplementary Information (ESI)

Table of contents:

1. Stability of Ru(II)-complexes in human plasma

The determination of the long-term stability of **Ru1** and **Ru2** in human plasma was perfomed by comparing their ^{1}H NMR spectra in phosphate buffer and in plasma samples at two different time points, i.e. 0 h and overnight (ON). The reference samples were obtained diluting 1:1 a solution of 100 µM of Ru1 or Ru2 with a sodium phospathe buffer (70 mM Na_2HPO_4; 6.1 mM NaN_3, pH 7.4). The plasma samples were created by pooling plasma of 5 different donors and diluted 1:1 with the above described sodium phosphate buffer added with 100 µM of **Ru1** or **Ru2**, as for standard NMR-based metabolomics of plasma[1,2]. The mixtures were homogenized by vortexing for 30 s and transferrred into 5.00 mm NMR tubes (Bruker BioSpin) for analysis. All ^{1}H NMR spectra were acquired using a Bruker 600 MHz spectrometer (Bruker BioSpin) at 310 K (again according to standard procedures for plasma NMR measurements).[1] One-dimensional ^{1}H NMR spectra with water peak suppression and a standard CPMG pulse sequence were recorded (512 scans, 73,728 data points, a spectral width of 12,019 Hz, and a relaxation delay of 4 s). Before applying Fourier transform, free induction decays were multiplied by an exponential function equivalent to a 0.3 Hz line-broadening factor. Transformed spectra were automatically corrected for phase and baseline distortions using TopSpin 3.5 (Bruker BioSpin). For clarity, here we show the aromatic portion of the spectra. Indeed, the aliphatic region of the spectra acquired in plasma are difficult to interpret, given the pH-dependent fluxionality of the compounds, and the more severe signal overlap.

.
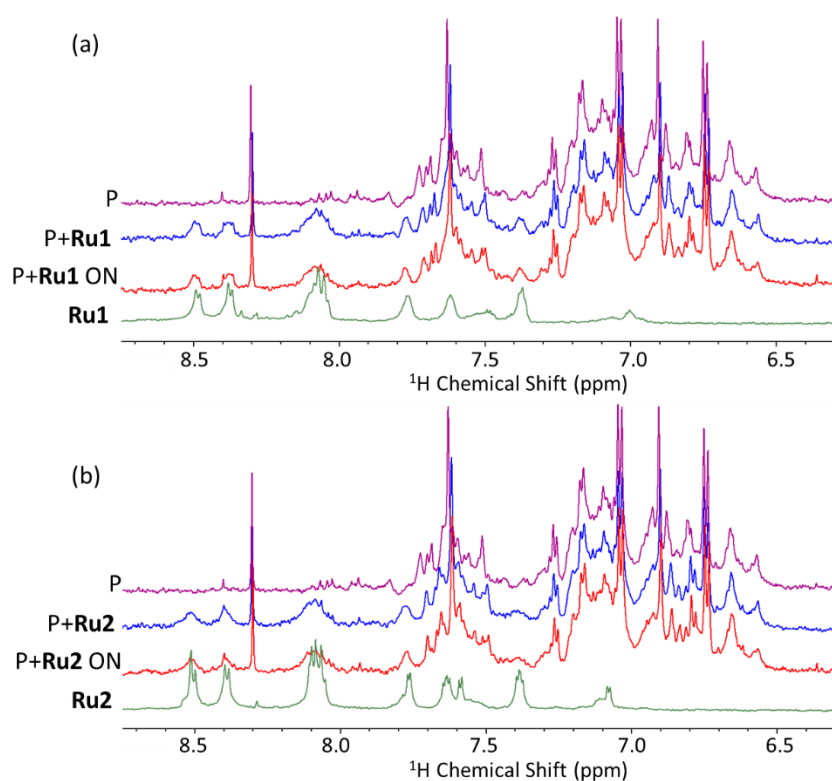
Fig. S1 ^{1}H NMR spectra acquired at 600 MHz (downfield region, 8.5-6.5 ppm) of **Ru1** (a) and of **Ru2** (b) in phosphate NMR buffer (pH 7.4) and in samples of plasma (P) (aromatic regions). Purple traces: raw plasma sample; blue traces: **Ru1/Ru2** in plasma sample, P+**Ru1**/P+**Ru2**, at the moment of the addition (t = 0); red traces: **Ru1/Ru2** maintained in plasma sample overnight (ON), P+**Ru1** ON or P+**Ru2** ON; green traces: **Ru1/Ru2** in NMR phosphate buffer.

2. Encapsulation of Ru(II)-polypyridyl complexes into ferritin cavity.

Fig. S2 Main structural features of human ferritin. (a) Cartoon representation of a ferritin cage composed by 24 subunits (PDB id: 5N27)[3]. The circle highlights the presence of one three-fold channel out of 8 that takes place where three subunits come in contact responsible for the ent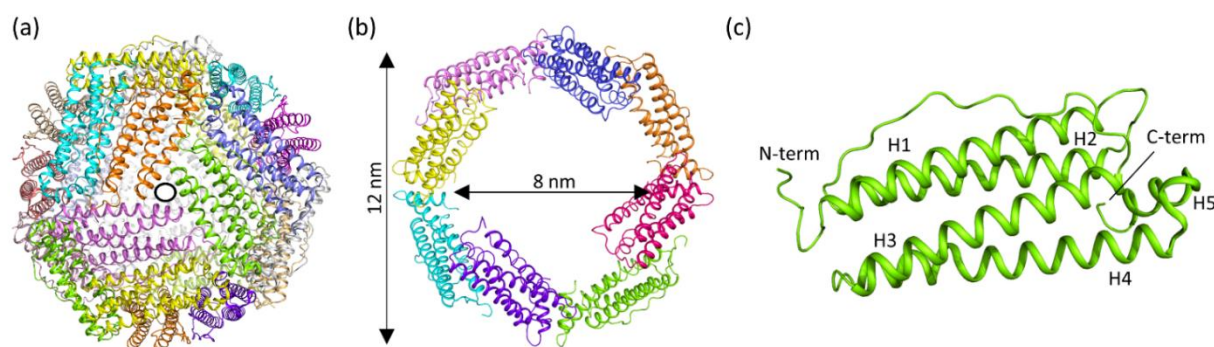ry of iron ions, as well as of other metal ions and small molecules. (b) Cavity view with external and internal diameter sizes. (c) 4-helix bundle structure of each ferritin subunit composed by 4 antiparallel α-helices (H1-H4) and a fifth smaller helix (H5) tilted with respect to the axis bundle. All helices are connected by small loops, while H2 and H3 are linked via a solvent exposed loop extending over the entire bundle length.
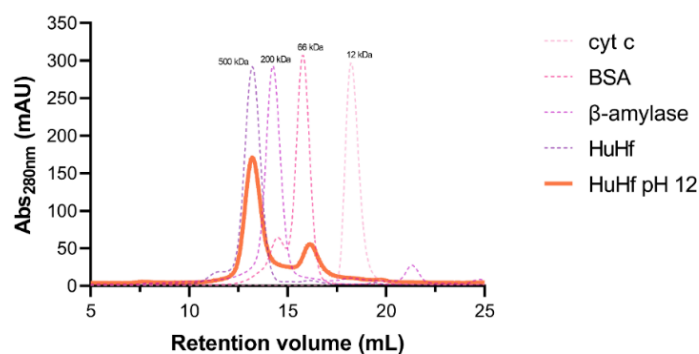

Fig. S3 Size exclusion analysis of ferritin sample treated at pH 12. HuHf was incubated at pH 12 simulating the disassembly process and then the sample was subjected to Superdex 200 10/300 GL size exclusion column. A series of protein standars with known molecular weights (cytochrome c from horse heart, 12.4 kDa; bovine serum albumin, 66 kDa; β-amylase from sweet potato, 200 kDa; human H-ferritin, 500 kDa) were eluted to obtain a calibration curve and determine the molecular mass of the protein species belonging to HuHf pH 12 sample. Comparing the ratio of V_e/V_o for the HuHf pH 12 sample to the V_e/V_o of protein standards (V_e is the elution volume and V_o is the void volume of the column), a species related to ferritin with 24-meric conformation and another one corresponding to smaller ferritin oligomer of about 60 kDa (probably indicating the presence of trimers) were found.
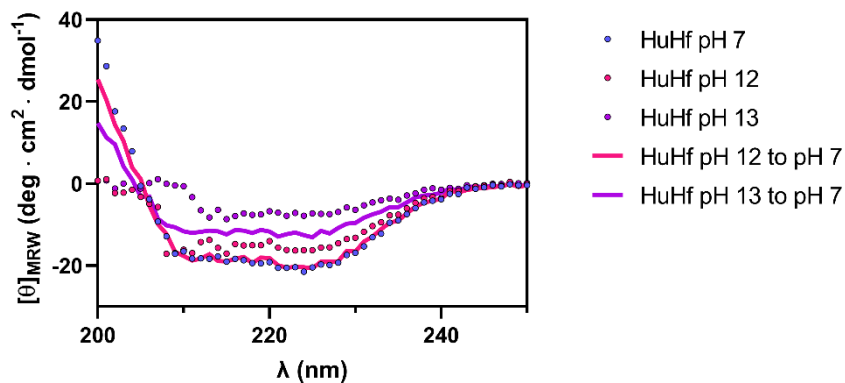
Fig. S4 Circular dichroism spectra of HuHf at different pH values. CD spectra were recorded in the far UV spectral window at 20 °C with a Jasco J-810 spectropolarimeter using a 0.1 cm path length quartz cuvette and 10 μM protein concentration (in subunits) in 50 mM sodium phosphate buffer (NaPi), pH 7. HuHf in NaPi buffer at pH 7 was taken as reference. HuHf samples at pH 12 and 13 were prepared adding NaOH 5 M to the solutions and incubated for 2 hours before CD spectra acquisition. Then, the pH of both samples was lowered to pH 7 and new CD spectra were recorded (HuHf pH 12 to pH 7 and HuHf pH 13 to pH 7 samples).

3. Characterization of Ru(II)-loaded ferritin structures

3.1 UV-visible and fluorescence characterization of Ru1@HuHf assemblies.

Fig. S5 Spectroscopic characterization of **Ru1** upon encapsulation into HuHf. (a) Combined UV-visible (50 µM **Ru1**) and fluorescence spectra of the reference compound **Ru1** and its correspondent encapsulated formula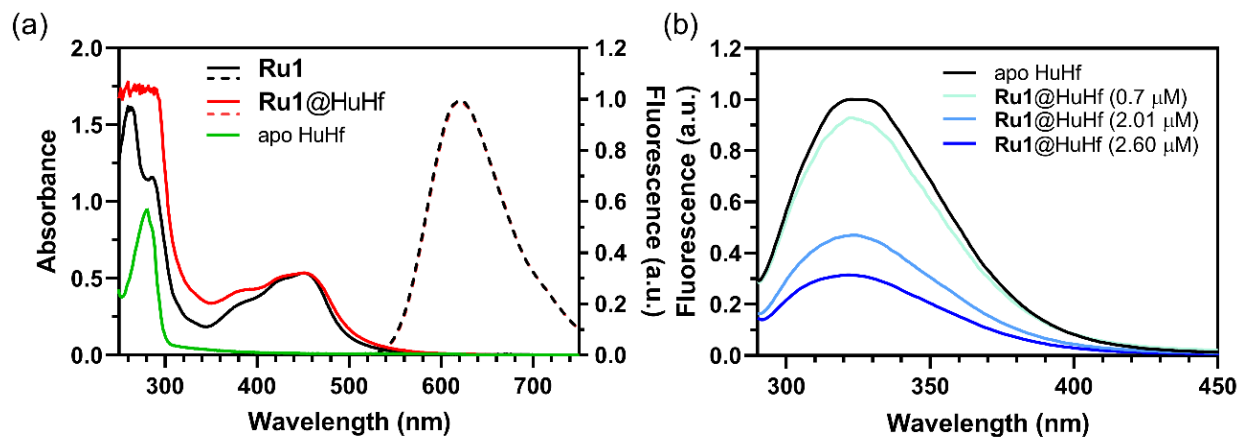tion (**Ru1**@HuHf), represented as straight and dotted lines respectively. Fluorescence was acquired at λ_{exc} 411 nm at constant **Ru1** concentration of 6 µM. UV-vis spectrum of apo HuHf is shown as control. (b) Intrinsic fluorescence of HuHf (0.32 µM), registered exciting at λ_{exc} 280 nm with increasing amount of **Ru1** (molar concentrations are in brackets). All experiments were performed in 50 mM sodium phosphate at pH 7 and room temperature.
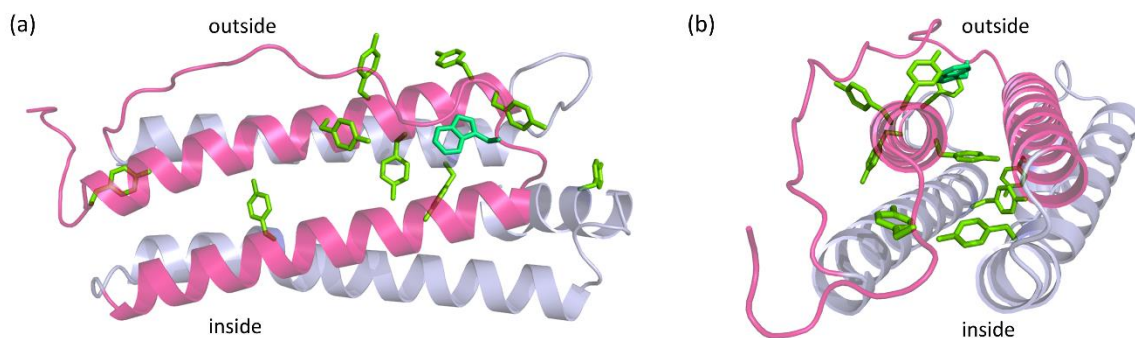
Fig. S6 Intrinsic fluorophores localization in H-ferritin subunit. (a) Top view and (b) side view of a human H-ferritin subunit (PDB id 5N27) represented as cartoon. The solvent-exposed elements are highlighted in magenta; the region of the α-helix bundle facing the internal cavity of the cage is indicated in light blue. The tyrosine (9) and the tryptophan (1) residues responsible for the intrinsic fluorescence registered at λ_{exc} 280 nm as shown in Fig. 2b and in Fig. S5b are shown as green and cyan stick, respectively.

3.2 ¹H NMR analysis of Ru-ferritin assemblies

High field ¹H NMR spectra of **Ru1**, **Ru2** (100 μM), apo HuHf (25 μM in cage) and of **Ru1**@HuHf and **Ru2**@HuHf (100 μM of **Ru1** and **Ru2** encapsulated) in phosphate NMR buffer (pH 7.4) were acquired and compared to further investigate the interaction of the encapsulated **Ru2** with HuHf (Fig. S5a,b). The one-dimensional ¹H NMR spectra were recordered on a Bruker 900 MHz spectrometer (Bruker BioSpin) at 298 K, using water peak suppression and a standard CPMG pulse sequence (3k scans, 102,400 data points, a spectral width of 19,167 Hz, acquisition time of 2.97 s, Hz and a relaxation delay of 4 s). This type of sequence has been used to selectively observe the sharp signals arising from the low molecular weight molecules free in solution and to suppress the broad resonances coming from ferritin. Before applying Fourier transform, free induction decays were multiplied by an exponential function equivalent to a 2.0 Hz line-broadening factor. Transformed spectra were automatically corrected for phase and baseline distortions using TopSpin 3.5 (Bruker BioSpin).

As shown in Fig. S7, the broadening beyoind detection of signals of **Ru1** and **Ru2** protons observed in the spectra of **Ru1**@HuHf (Fig. S7a) and of **Ru2**@HuHf (Fig. S7b) is consistent with the interaction of the metal complexes with HuHf, confirming the evidences gained from fluorescence/SAXS measurements. Furthermore, are reported the spectra of **Ru1** and **Ru2** added directly in a solution of apo HuHf at neutral pH; here, the resonances belonging to the ligands are visible in the spectra with line widths comparable to those of the respective isolated complex, confirming that the interaction does not occur on the external surface of the protein.
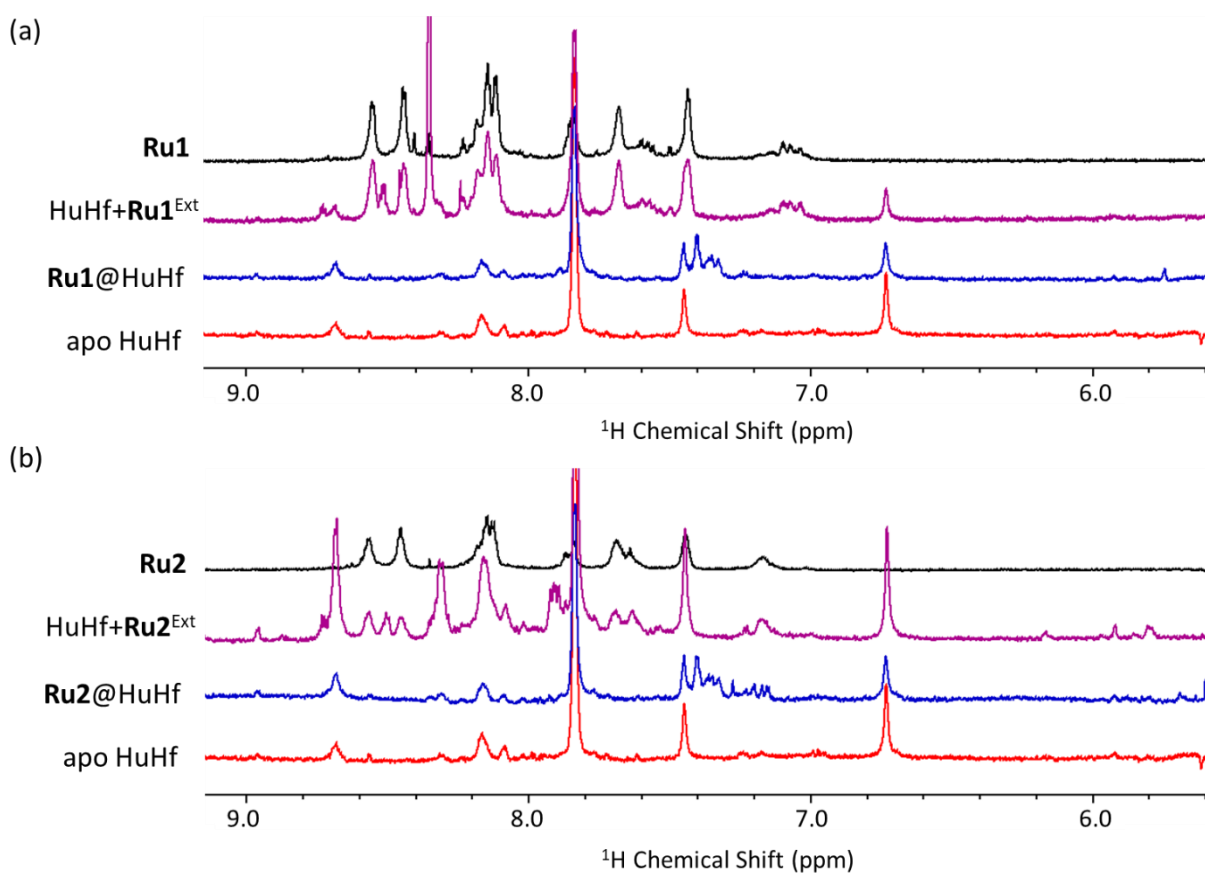
Fig. S7 Downfield region (10.00-6.00 ppm) of the ¹H NMR spectra acquired at 900 MHz in phosphate NMR buffer (pH 7.4). Spectra of a) **Ru1** and b) **Ru2**, black traces compared with: the spectra of their encapsulated forms (**Ru1**@HuHf and **Ru2**@HuHf respectively), blue traces; and with **Ru1** and **Ru2** in a solution added with intact apo HuHf, purple traces. The spectrum of apo ferritin (apo HuHf) in the absence of the Ru-compounds, red traces.

3.3 Determination of Ru1@HuHf and Ru2@HuHf structural stability by circular dichroism analysis.

The secondary structure stability of **Ru1**@HuHf and of **Ru2**@HuHf nanosystems was determined by circular dichroism analysis looking at the two negative maxima around 208 and 220 nm relative to α-helical elements. In fact, as shown in Fig. S2, each HuHf subunit features an α-helix bundle conformation. Temperature dependence measurements were performed on a wide range (25-85°C) due to the peculiar thermal stability of apo HuHf. The resulting CD spectra are reported in Fig. S8.
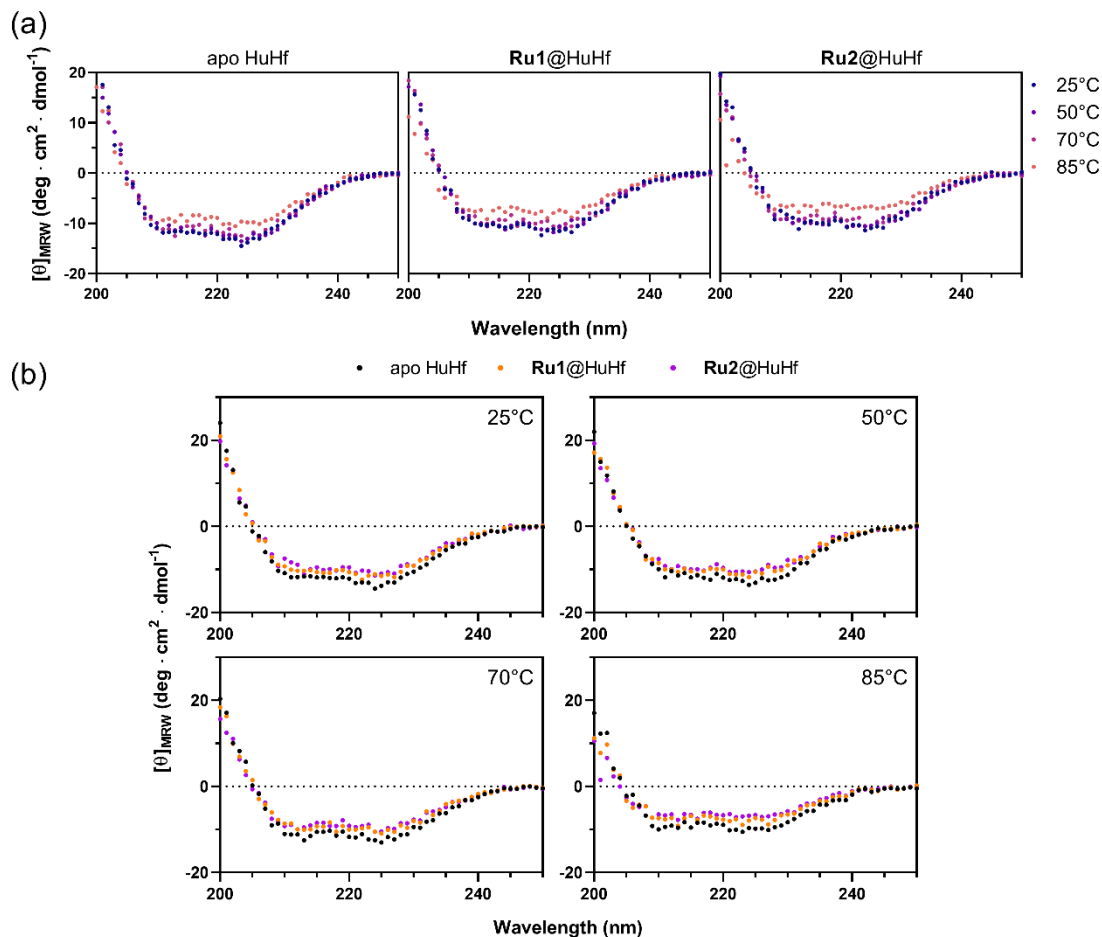

Fig. S8 Circular dichroism curves of **Ru1**@HuHf and of **Ru2**@HuHf in comparison with apo HuHf. (a) CD spectra of apo HuHf, **Ru1**@HuHf and **Ru2**@HuHf acquired at 25°C, 50°C, 70°C and 85°C in the far-UV. (b) Superimposition of all samples spectra in separated panels (one for each temperature condition) to make easier visualizing the slight differences of **Ru1**@HuHf and **Ru2**@HuHf with respect to the apo protein.

3.4 Determination of apo HuHf, Ru1@HuHf, Ru2@HuHf nanostructures by small angle X-ray scattering (SAXS).

SAXS is a useful tool to assess the size and internal structure of colloids and protein solutions in the size range from 1 to about 100 nm. SAXS technique characterizes changes at the nanometer scale in situ and often in a non-destructive way. SAXS is therefore essential for investigating the conformational changes occurring in biomolecules and especially in the tertiary and quaternary structural levels of proteins.[4,5]

SAXS signal is the Fourier transform of the electron density contrast between the different sample constituents. When the system is diluted the inter-particle interference can be neglected and the only correlation remaining comes from the intra-aggregate topology, also called form factor F(q). Thus, the scattered intensity can be calculated as *I(q) =|F(q)|² + bkg*. For a monodisperse core-shell system, I(q) takes the analytical form:

$$I(q) = \frac{scale}{V_{shell}} \left[\frac{3V_c(\rho_c - \rho_{shell})j_1(qR_c)}{qR_c} + \frac{3V_s(\rho_{shell} - \rho_{solv})j_1(qR_{shell})}{qR_{shell}} \right]^2 + bkg \qquad \text{(Eq. S1)}$$

where $j_1(x) = (sinx - xcosx)/x^2$ is the Bessel function of the first kind, R_c is the radius of the core, $R_{shell} = R_c + t$, t is the thickness of the shell, ρ_i and $V_i = (4\pi/3)R_i^3$ (with i = c, *shell* and *solv*) are the electron densities and volumes of the different regions of the system (i.e. core, shell and solvent), *bkg* is an instrumental background and *scale* is the product of

the particle volume fraction with the instrumental efficiency.[6] For a hollow protein cage, like in the case of the apo HuHf, $\rho_c = \rho_{solv}$.

Eq. S1 was used to model the SAXS patterns reported in Fig. 2c with ρ_{solv} = 9.4 x 10^{-6} Å^{-2} the electron density of the buffer solution and allowing ρ_c, ρ_{shell}, the geometrical parameters (R_c, t), *scale* and *bkg* to vary. Best fitting results were obtained when $\rho_c = \rho_{solv}$ even in the case of **Ru1**@HuHf and **Ru2**@HuHf confirming that the quaternary structure of the protein is completely recovered after reassembly. Associated fitting parameters are listed in Table 1 of the manuscript and ρ_{shell} resulted around 1.18 x 10^{-5} Å^{-2} (i.e. the scattering length density expected for the apo ferritin).[7] The modeling procedures were performed in IGOR Pro 7.0 using the macros contained in the SANS analysis 4.0 package.[8]

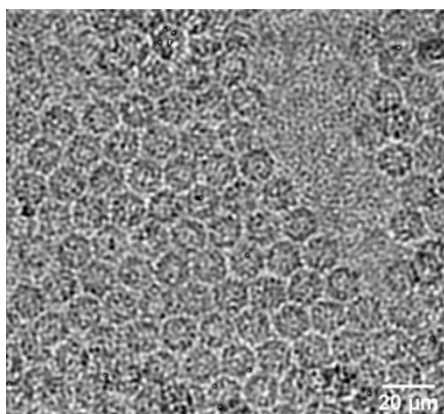### 3.5 Intactness of the cage structure by cryo-EM

Fig. S9 Representative Cryo-EM micrographs of apo HuHf. Holey-carbon R1.2/1.3 grids (Quantifoil Micro Tools GmbH) covered by 2 nm film of carbon were prepared. Grid surfaces were treated with plasma cleaning using a O2 for 45 s before applying 3 μL of sample (1 mg/mL apo HuHf in PBS buffer at pH 7.4). Grids were blotted in 100% humidity and 10 °C with filter paper and vitrified by rapidly plunging into liquid ethane at −180 °C using a Vitrobot Mark IV (FEI, Hillsboro). Screening analysis on vitrified samples was performed by a ThermoFisher Glacios at 200-kV instrument equipped with a Falcon III direction electron detector.

4. Singlet Oxygen Detection.

The ability of Ru(II)-nanocomposites to sensitize $^1O_2$ formation upon light-activation was assessed employing indirect chemical trapping methods involving the use of water-soluble substrates selective for $^1O_2$ (*vide infra*).

In all subsequent experiments, irradiation was performed by exposing air-saturated aqueous samples to visible light (LED Lamp, 30 W, λ > 430 nm) for regular intervals of time.

4.1 Photochemical Stability of Ru1 and Ru2.

Prior to study the $^1O_2$ sensitizing properties of 'free' and protein-encapsulated Ru(II)-complexes, photochemical stability tests were performed in order to assess the stability of ruthenium complexes in aqueous solutions under prolonged irradiation times. To this aim, air-saturated aqueous solutions of **Ru1** and **Ru2** buffered at neutral pH were irradiated and then we collected the relative UV-vis absorption spectra every 30 min for 2 hours. As shown in Fig. S10, the UV-vis absorption spectra registered at different irradiation times did not show significant variations, thus indicating the photostability of both compounds under these experimental conditions.
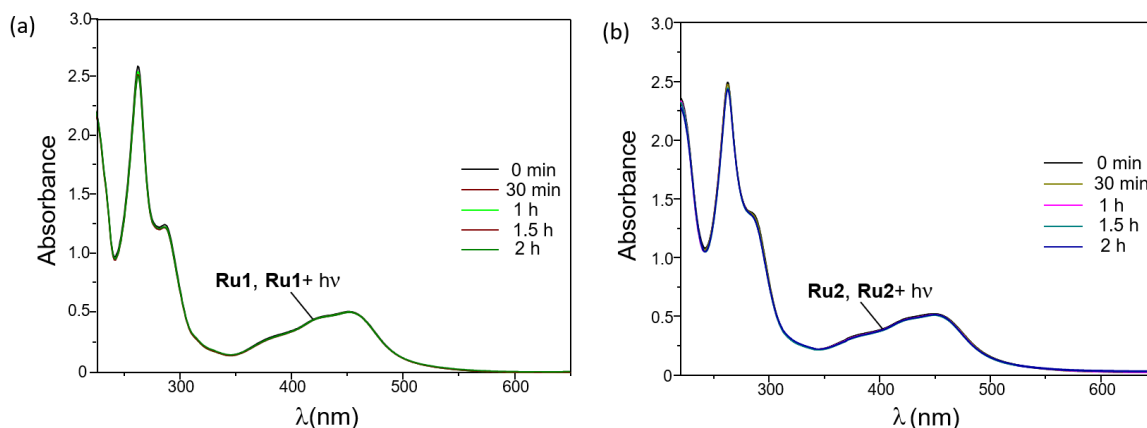

Fig. S10 UV-vis absorption spectra of air-saturated aqueous solutions of **Ru1** (a), and **Ru2** (b) at neutral pH collected at different irradiation times. ([**Ru1**] = 3 x 10^{-5} M, [**Ru2**] = 4 x 10^{-5} M, 50 mM sodium phosphate pH 7 buffer).

4.2 Singlet oxygen determination by 1,5-Dihydroxynaphthalene (DHN).

The capacity of Ru(II)-based photosensitizers (**Ru1**, **Ru2**, **Ru1**@HuHf and **Ru2**@HuHf) to produce singlet oxygen ($^1O_2$) upon light-activation was firstly studied by employing the chemical probe 1,5-dihydroxynaphthalene (DHN), as indirect reporter of $^1O_2$. In fact, DHN is promptly and quantitatively oxidized by $^1O_2$ to give 5-hydroxy-1,4-naphthalenedione (Juglone), according to Equation S2 and Scheme S1:[9]

$$DHN + \; ^1O_2 \rightarrow Juglone \; + \frac{1}{2} \; ^3O_2 \quad (Eq. \; S2)$$
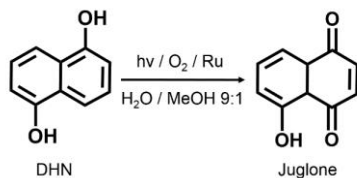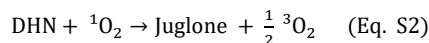
Scheme S1. Photochemical conversion of DHN to Juglone.

This photo-oxidation process can be easily monitored by means of UV-visible spectroscopy, following the decrease of the DHN absorption band at λ_{max} 297 nm, and the simultaneous increase of the broad Juglone band, centered at c.ca 427 nm.
By considering the short reaction time and the instantaneous interaction between DHN and $^1O_2$ to form Juglone, it is possible to apply the steady-state approximation to the $^1O_2$ intermediate. In these conditions, the disappearance rate of $^1O_2$ coincides with the DHN consumption, and the rate of the photo-oxidation can be assumed to be first order in DHN, as shown in Equation S3.

$$\upsilon = -\frac{d[^1O_2]}{dt} = -\frac{d[DHN]}{dt} = k_{obs}[DHN] \quad (Eq. \, S3)$$

Since the absorbance at 297 nm (A_{297}) can be unequivocally attributed to DHN, under the experimental conditions employed, the rate constants (K_{obs}) for the photo-oxidation of DHN by the different photosensitizers can be obtained by fitting the experimental A_{297} absorbance values by using the following equation (Equation S4):

$$\ln \frac{[DHN]_t}{[DHN]_0} = \ln \frac{(A_{297})_t}{(A_{297})_0} = -k_{obs} \, t \quad (Eq. \, S4)$$

where $[DHN]_0$ and $[DHN]_t$ are the molar concentration of DHN at time 'zero' and at a generic time 't', while $A_{(297)0}$ and $A_{(297)t}$ are the correspondent absorbance values measured at 297 nm.
In Fig. S11 are reported the UV-vis spectra of aqueous solution of DHN (3.3 x 10^{-4} M) at pH 7 recorded in the absence, and in the presence of 10 µM of **Ru1**, **Ru2**, [Ru(phen)$_3$]$^{2+}$ and **Ru1**@HuHf, obtained for increasing irradiation times. The spectra obtained for the probe in the presence of **Ru2**@HuHf are reported in Fig. 3a of the manuscript. We highlight that the presence in these spectra (unless in those acquired in the absence of PSs (Fig. S11a) of two clear isosbestic points at ca. 280 and 330 nm rules out the possible formation of by-products or long-lived intermediates.
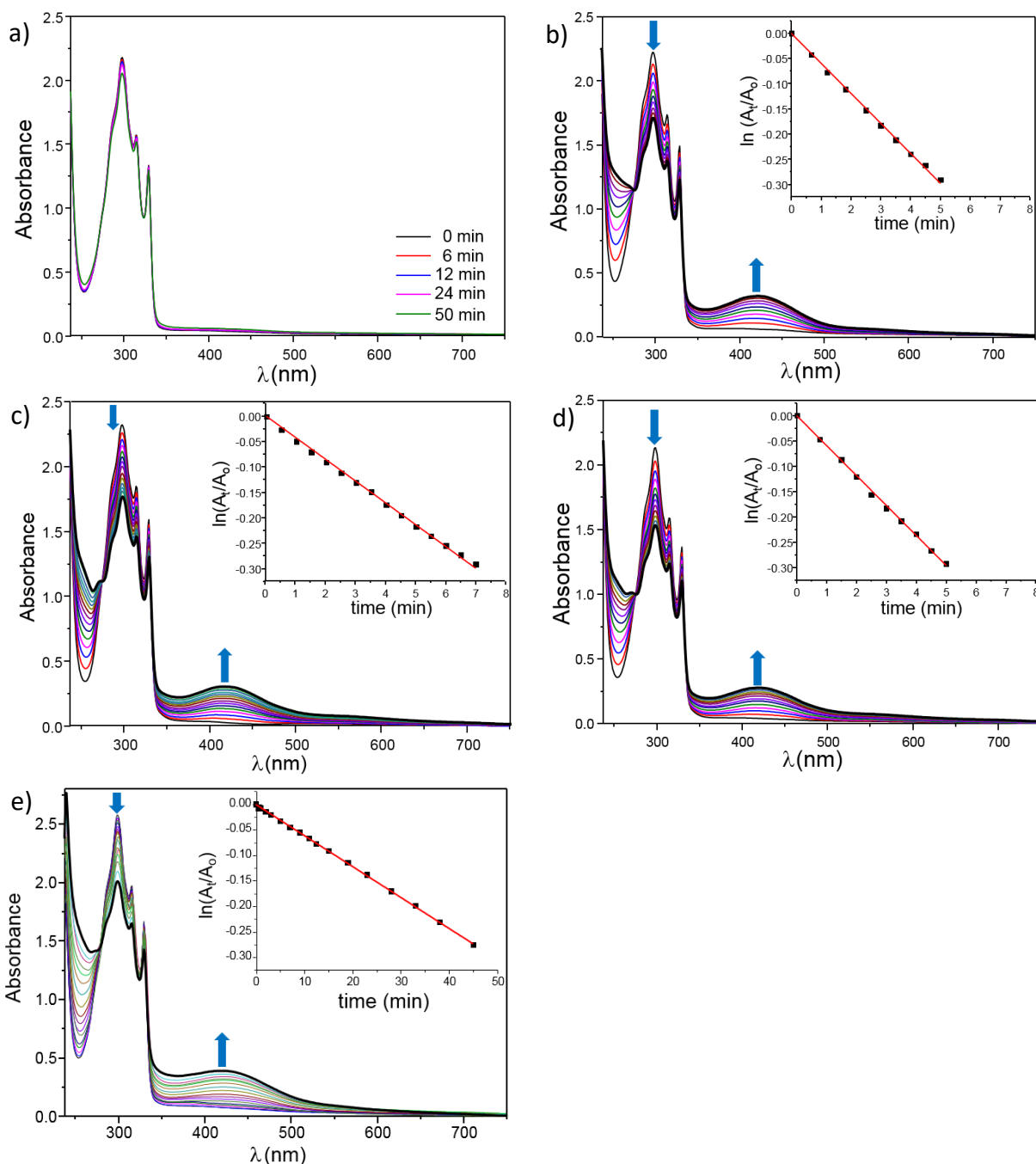
Fig. S11 Absorption spectra of aqueous solutions of DHN irradiated with LED light ($\lambda > 430$ nm) for different times in the absence (a) and in the presence of [Ru(phen)$_3$]$^{2+}$ (b), **Ru1** (c), **Ru2** (d) and **Ru1**@HuHf (e). On top right of figures (b), (c), (d) and (e) are reported the correspondent semilogarithmic plots of ln(A_t/A_o) plotted as a function of the irradiation time. ([DHN] = 3.3 x 10^{-4} M, [PS] = 10 µM, pH 7).

4.3 Singlet oxygen determination by the Singlet Oxygen Sensor Green (SOSG) reagent. The $^1O_2$ sensitizing abilities of free ruthenium compounds and Ru(II)-nanosystems was further evaluated by monitoring the green fluorescence emission from the Singlet Oxygen Sensor Green reagent (SOSGR) (Invitrogen).[10] This reagent is in fact largely used for the $^1O_2$ detection in aqueous solutions, due to its high selectivity for $^1O_2$ without showing appreciable responses to hydroxyl radicals or superoxide ions.[11] In its intact form, this probe appears to be basically fluorescently quenched (it only displays a weak blue fluorescence with excitation peaks at 372 and 393 nm and emission maxima centered at 395 and 416 nm). The interaction with $^1O_2$ determines an intense green fluorescence emission, similarly to that of fluorescein (excitation/emission maxima c.ca 504/525 nm). As a result, the $^1O_2$ production from a selected PS agent can be easily monitored by following the fluorescence emission of SOSG at 525 nm (I_{exc} = 488 nm).

Samples have been prepared as described in the experimental section of the manuscript. Two controls were analyzed, one containing a mixture of SOSGR and [Ru(phen)$_3$]$^{2+}$ maintained under dark conditions, and the other one consisting of only the probe exposed to different irradiation times. The latter control was measured in order to take into account of the modest, but generally not negligible,

photosensitizing property of SOSG itself when exposed to visible radiation.[12] However, this contribute appears to be overestimated under our experimental conditions because of the rather modest $^1O_2$ quantum yield of SOSG in aqueous media (Φ_Δ = 0.006 ± 0.002 and 0.002 ± 0.001 for excitation at 355 and 532 nm in D_2O:MeOH 95:1)[12–14] and in consideration of the low molar ratio employed with respect to the ruthenium compound ([Ru]/[SOSG] = 10:1). The results obtained are shown in Fig. 3b of the manuscript.

5.1 TfR1 expression in C2C12, HeLa and A2780 cells by confocal immunofluorescence analysis.

The localization of TfR1 was evaluated by confocal immunofluorescence analysis in non-permeabilized cells (C2C12 myoblasts, HeLa and A2780 cancer cell lines) to assess plasma membrane distribution of the receptor, using specific anti-TfR1 antibody. This receptor is in fact largely expressed in cancer rather than non-cancer cells, as already reported,[15,16] and can account for the selective internalization of ferritin nanocarrier in tumor cells. Immunofluorescence analysis of TfR1 was performed in different culture condition, in order to verify TfR1 distribution in proliferative cells compared to serum-starved cells for 1 and 24 hours, that represent times of incubation in serum deprived medium before ferritin-Ru(II) nanocage administration and photoactivation, respectively.
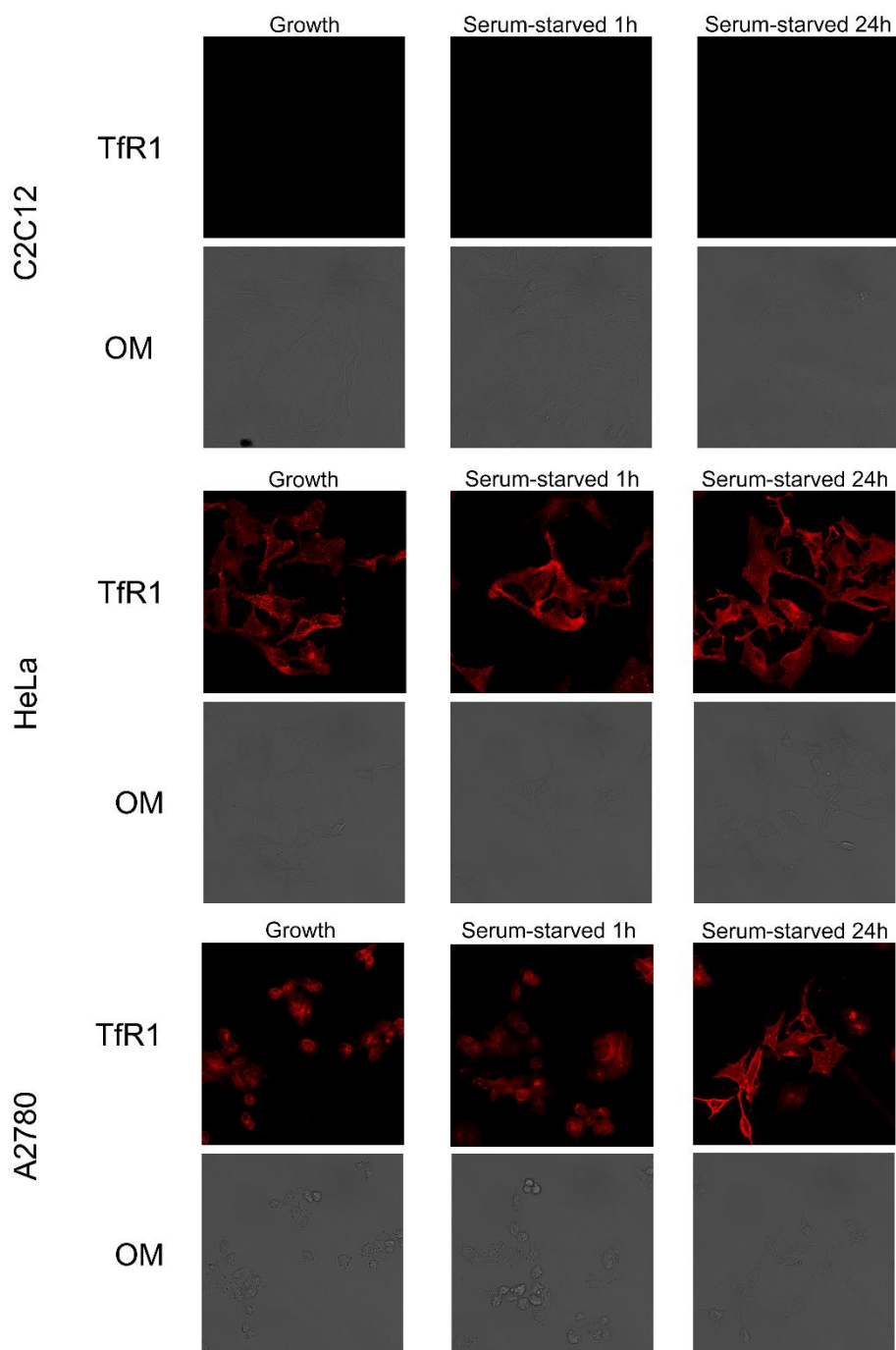
Fig. S12 Confocal immunofluorescence analysis of TfR1 expression in C2C12 HeLa and A2780 cells. Laser scanning confocal microscopy immunofluorescence analysis was performed in C2C12 myoblasts, HeLa and A2780 cells under different culture conditions. Cells were seeded in microscope slides and incubated in 10% FBS supplemented growth medium (growth) or serum-deprived medium supplemented with 0.1% BSA for 1 hour and 24 hours (serum-starved 1h or 24h). After fixation in 2% paraformaldehyde, specific anti-TfR1 primary antibody followed by secondary anti-mouse antibody conjugated with Texas red (red) was incubated in non-permeabilized cells. Representative confocal microscope images show the localization of TfR1 at plasma membrane (upper panel) and the corresponding optical microscopy images (OM).

5.2 Cell internalization and colocalization of Ru(II) nanocages, Ru1@HuHf e Ru2@HuHf, with TfR1 in A2780 cells by confocal immunofluorescence analysis.

Cell internalization of Ru(II)-ferritin nanocages with TfR1 by A2780 cells was studied using intrinsic fluorescence properties of Ru(II) ligands and immunofluorescence analysis, employing specific anti-TfR1 antibodies. Fig. S13 shows the distribution of **Ru1**@HuHf and **Ru2**@HuHf in intracellular compartments (red), the cellular localization of TfR1 (green) and colocalization of Ru(II)-ferritin nanocages together with TfR1 (merge).
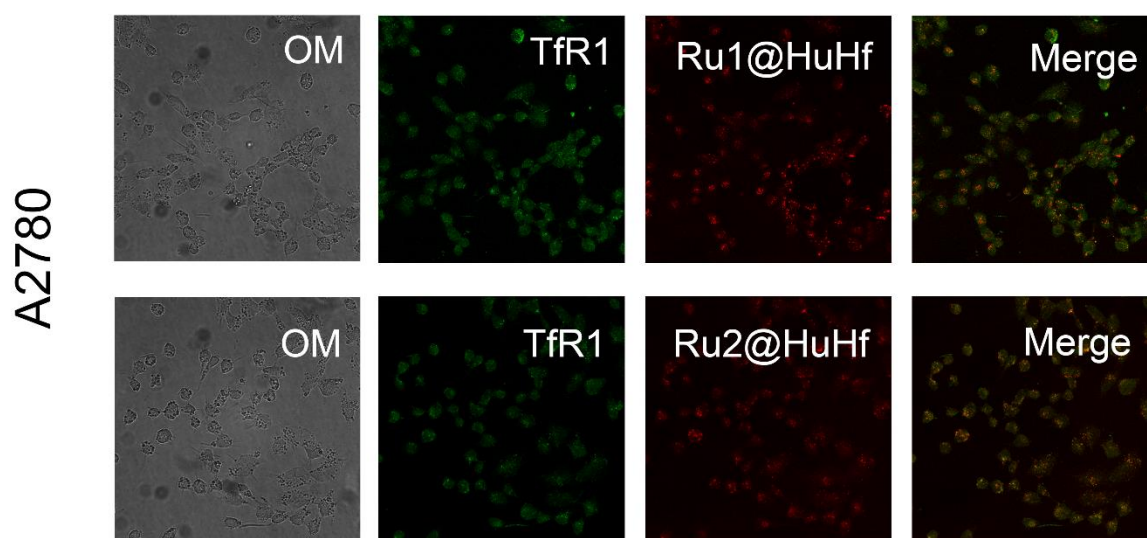

Fig. S13 Confocal immunofluorescence analysis of Ru(II) nanocages, Ru1@HuHf e Ru2@HuHf, and TfR1 in A2780 cells. Laser scanning confocal microscopy was performed in A2780 cells incubated with each Ru(II) nanocomposite, **Ru1**@HuHf and **Ru2**@HuHf (10 µM) for 24 hours. Immunofluorescence analysis was performed by using specific anti-TfR1 primary antibody and secondary anti-mouse antibody conjugated with fluorescein (green) in permeabilizad cells. Ru(II) nanocages display fluorescent properties: Ex λ=440–480 nm and Em λ=600–640 nm (red). Confocal microscopy images are representative of three indipendent experiments, that show the distribution of TfR1 and Ru(II) nanocomposites, as well as colocalization (right panel, merge) and the corresponding optical microscopy images (left panel, OM).

5.3 Dose-dependent activity of non-encapsulated Ru1 and Ru2 complexes toward HeLa, A2780 and non cancer C2C12 cell lines.

The cytotoxic effects of free, non encapsulated ruthenium compounds **Ru1** and **Ru2** against both cancer (HeLa and A2780) and non cancer (C2C12) cell lines, was also investigated. To this aim, cells were incubated for 48 h in the presence of **Ru1** and **Ru2** at concentrations of 0, 1, 10 and 40 µM in serum-deprived culture media (supplemented with BSA 0.1%) under dark. The cellular viability of the different cell lines was then evaluated through MTT reduction analysis and performing each measurement in triplicate. The obtained results are reported in the following Fig. S14.
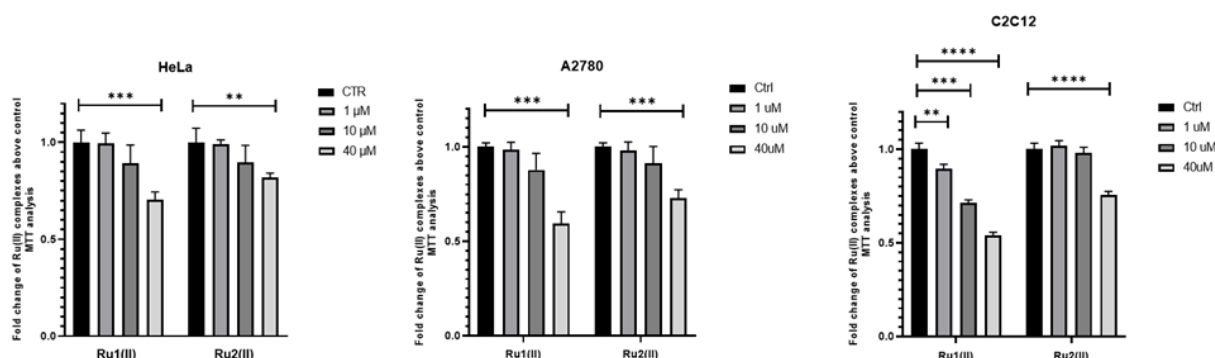
Fig. S14 Dose-dependent activity of non-encapsulated Ru1 and Ru2 compounds assessed by MTT assay. Cellular viability of different cancer (HeLa and A2780) and non-cancer (C2C12) cell lines was assessed by MTT reduction analysis in the presence of different concentrations of ruthenium compounds **Ru1** and **Ru2**. MTT analysis was performed following incubation of cells in the absence and in the presence of Ru(II)-complexes at concentrations of 1 µM, 10 µM and 40 µM in serum-deprived culture media (supplemented with BSA 0.1%) for 24 h, under dark. Experiments were performed in triplicate, representative of three independent ones with similar results. Data reported are mean ± SEM of fold change absorbance at 570 nm in cells dosed with different Ru(II) concentrations to control sample. The effect of Ru(II) compounds on the inhibition of cell survival was statistically significant by 1-way ANOVA followed by Bonferroni post-hoc test. $**P<0.01$, $***P<0.001$, $****P<0,0001$.

References

1 A. Vignoli, V. Ghini, G. Meoni, C. Licari, P. G. Takis, L. Tenori, P. Turano and C. Luchinat, High-Throughput Metabolomics by 1D NMR, *Angew. Chem. Int. Ed Engl.*, 2019, **58**, 968–994.

2 P. G. Takis, V. Ghini, L. Tenori, P. Turano and C. Luchinat, Uniqueness of the NMR approach to metabolomics, *TrAC Trends Anal. Chem.*, 2019, **120**, 115300.

3 G. Ferraro, S. Ciambellotti, L. Messori and A. Merlino, Cisplatin Binding Sites in Human H-Chain Ferritin, *Inorg. Chem.*, 2017, **56**, 9064–9070.

4 S. Doniach, Changes in Biomolecular Conformation Seen by Small Angle X-ray Scattering, *Chem. Rev.*, 2001, **101**, 1763–1778.

5 D. Sato, H. Ohtomo, Y. Yamada, T. Hikima, A. Kurobe, K. Fujiwara and M. Ikeguchi, Ferritin Assembly Revisited: A Time-Resolved Small-Angle X-ray Scattering Study, *Biochemistry*, 2016, **55**, 287–293.

6 A. Guinier, G. Fournet and C. B. Walker, SCATTERING OF X-RAYS.

7 V. I. Petrenko, M. V Avdeev, V. M. Garamus, O. I. Ivankov and L. A. Bulavin, Effect of iron oxide loading on magnetoferritin structure in solution as revealed by SAXS and SANS, 2014, **123**, 82–88.

8 S. R. Kline, Reduction and analysis of SANS and USANS data using IGOR Pro, 2006, 895–900.

9 S. Y. Takizawa, R. Aboshi and S. Murata, Photooxidation of 1,5-dihydroxynaphthalene with iridium complexes as singlet oxygen sensitizers, *Photochem. Photobiol. Sci.*, 2011, **10**, 895–903.

10 C. Flors, M. J. Fryer, J. Waring, B. Reeder, U. Bechtold, P. M. Mullineaux, S. Nonell, M. T. Wilson and N. R. Baker, in *Journal of Experimental Botany*, 2006.

11 A. Prasad, M. Sedlářová and P. Pospíšil, Singlet oxygen imaging using fluorescent probe Singlet Oxygen Sensor Green in photosynthetic organisms, *Sci. Rep.*, 2018, **8**, 1–13.

12 X. Ragàs, A. Jiménez-Banzo, D. Sánchez-García, X. Batllori and S. Nonell, Singlet oxygen photosensitisation by the fluorescent probe Singlet Oxygen Sensor Green®, *Chem. Commun.*, 2009, 2920–2922.

13 R. Schmidt, C. Tanielian, R. Dunsbach and C. Wolff, Phenalenone, a universal reference compound for the determination of quantum yields of singlet oxygen O2(1Δg) sensitization, *J. Photochem. Photobiol. Chem.*, 1994, **79**, 11–17.

14 F. Wilkinson, W. P. Helman and A. B. Ross, Quantum Yields for the Photosensitized Formation of the Lowest Electronically Excited Singlet State of Molecular Oxygen in Solution, *J. Phys. Chem. Ref. Data*, 1993, **22**, 113–262.

15 T. R. Daniels, T. Delgado, G. Helguera and M. L. Penichet, The transferrin receptor part II: Targeted delivery of therapeutic agents into cancer cells, *Clin. Immunol.*, 2006, **121**, 159–176.

16 S. M. Jeong, S. Hwang and R. H. Seong, Transferrin receptor regulates pancreatic cancer growth by modulating mitochondrial respiration and ROS generation, *Biochem. Biophys. Res. Commun.*, 2016, **471**, 373–379.